Strengthening mechanisms of an Al-Mg-Sc-Zr alloy

K.L. Kendig *, D.B. Miracle

Air Force Research Laboratory, Materials and Manufacturing Directorate, 2230 Tenth Street, Wright-Patterson AFB, OH 45433-7817, USA

Abstract

As a step toward developing an Al-Mg-Sc-Zr alloy for use up to 200 °C, the mechanisms responsible for alloy strengthening were identified for Al-6Mg-2Sc-1Zr (wt%) (Al-6.7Mg-1.2Sc-0.3Zr (at%)). The current work quantifies the active strengthening mechanisms at room temperature and explicitly considers solid solution strengthening, grain boundary strengthening, and $Al_3(Sc,Zr)$ precipitate strengthening. Existing strengthening models, together with data from microstructural characterization were used to determine the magnitude of individual contributions. Strengthening due to the sub-micron grain size was the largest contribution to alloy strength, followed in decreasing order by precipitate strengthening and solid solution strengthening. Tensile yield strengths, 540–640 MPa (78–93 ksi), measured at room temperature agree well with predicted values. Model predictions showed that increasing the precipitate size from 7.5 nm to 20–25 nm and increasing the volume fraction of these particles from 0.015–0.025 up to 0.035 could produce a material with a yield strength of 865 MPa (125 ksi). Published by Elsevier Science Ltd. on behalf of Acta Materialia Inc.

Keywords: Aluminium; Microstructure; Mechanical properties; Scandium

1. Introduction

Traditional aluminum alloys for high performance applications, such as Al 7075, have maximum use temperatures in the 150–170 °C range. Above this, alloy strength degrades quickly with time in service due to rapid coarsening of fine strengthening precipitates. Applications that have a maximum use temperature above this range are required to use a material with a much higher density, such as titanium or steel. The capability of utilizing an aluminum alloy in such applications would result in significant weight savings and likely a reduction in both cost and lead time for component production.

Significant past research has been conducted to develop new Al alloys with good high temperature properties. Many of the approaches included non-age-hardenable systems with thermodynamically stable precipitates for high temperature strength. Significant improvements were shown for sytems such as Al-Fe-Ce [1] and Al-Fe-V-Si [2,3], where the principle strengthening phases are incoherent intermetallic particles. An alternate approach is to use coherent intermetallic precipitates for strengthening. Only a limited number of possibilities exist in Al-based alloys for the formation of coherent

* Corresponding author. Tel: +1 937 255 1317; fax: +1 937 255 3007.

E-mail address: Kevin.kendig@wpafb.af.mil (K.L. Kendig).

strengthening particles that are thermodynamically stable and have the ordered, $L1_2$ structure [4]. Of the possibilities, additions of Er and Sc have been most commonly studied [4,5]. Er additions form the $L1_2$-ordered Al_3Er phase. While Er is less expensive than Sc and has a smaller freezing range, the lattice constant, approximately 0.422 nm [4], is significantly larger than that of Al, so that it is difficult to retain particle coherency to a useful size. Further, the density of Er-containing alloys is significantly higher than comparable alloys based on Sc.

Aluminum forms a thermodynamically stable Al_3Sc phase with scandium additions [6]. Sc has a very low solid solubility in Al, approximately 0.4 wt% at the eutectic temperature [6]. For this reason, solutionizing near the eutectic temperature followed by quenching to re-precipitate fine, dispersed Al_3Sc particles would be largely ineffective. The lattice parameter of the Al_3Sc phase, 0.410 nm [7], matches very closely to that of the aluminum matrix, 0.405 nm. Al_3Sc has the $L1_2$-type ordered face-centered cubic structure and should form coherent precipitates below a size of approximately 50 nm. The similarity of the lattice parameter and structure of Al_3Sc to those of the aluminum matrix is expected to reduce the driving force for coarsening of the Al_3Sc particles. Fine Al_3Sc precipitates that are coherent with the matrix are expected to contribute to the alloy strength through dislocation-particle interactions, as is the case in nickel-based superalloys. Addition of magnesium provides both solid solution strengthening and increases the lattice parameter of the aluminum matrix, which provides a better match with Al_3Sc and further decreases the driving force for coarsening of the Al_3Sc particles. It has been found that zirconium substitutes for Sc in Al_3Sc in up to 1/3 of the Sc lattice sites [7]. It is believed that as a slow diffuser in aluminum, the zirconium will additionally stabilize these $Al_3(Sc,Zr)$ precipitates.

Much of the earlier work on Al-Sc alloys has focused on hypoeutectic compositions, i.e., Sc contents below the Al-Sc binary eutectic composition of 0.36 at% (0.6 wt%) [4,7,8,9]. More recent work by Ünal and Kainer [10] has begun to investigate the behavior of hypereutectic compositions. However, many questions must be addressed to guide

in the efficient development of hypereutectic Al-Sc alloys for structural applications. The most fundamental questions relating to the magnitude of contributions by the various possible strengthening mechanisms has not been systematically addressed. The potential for further improvements, and the microstructural and compositional approaches which might be required to produce these improvements, have not been clearly discussed in the open literature.

In addition to the development of Al alloys with improved strength at elevated temperatures, a persistent and pervasive requirement exists for Al alloys with higher specific strength and stiffness at temperatures currently satisfied by existing Al alloys. While such alloys are typically used from room temperature to ~150 °C, Al alloys are sometimes used in cryogenic applications. For example, efforts are now underway to improve the specific strength of metals used for advanced liquid rocket engine static and dynamic components. The known characteristics of Al-Sc alloys, including potent grain refinement, suggest that such alloys could also be useful below room temperature. Once again, a clear understanding of the specific magnitudes of contributions from the various strengthening mechanisms, such as solid solution, particulate strengthening, and grain size refinement, is required to effectively lead an effort to develop and optimize advanced Al alloys for such applications.

The objective of the current work is to extend the effort to develop hypereutectic Al-Sc alloys as a class of high strength, high temperature structural materials. Following earlier work [1], Al-2Sc (wt%) is chosen as a base, and Mg has been added to reduce the density (thus increasing the density-normalized properties) and to reduce the lattice mismatch between the Al and Al_3Sc phases. Zr has been added to reduce the coarsening kinetics [7]. In addition, Zr forms a metastable $L1_2$ Al_3Zr precipitate, and so it is suggested that Zr may substitute for Sc in the Al_3Sc phase [7]. The current work quantifies the active strengthening mechanisms at room temperature and explicitly considers solid solution strengthening, grain boundary strengthening, and precipitate strengthening. Data from detailed microstructural characterization were used with available strengthening models to determine

the magnitude of individual contributions. These calculated contributions have been compared to room temperature mechanical results.

2. Experimental

An Al-6Mg-2Sc-1Zr (wt%) (Al-6.7Mg-1.2Sc-0.3Zr (at%))(all compositions will be in wt% unless noted otherwise) alloy was prepared via a powder metallurgy route. Powder was produced by helium atomization. Two materials were prepared from this powder; one with a <45μm particle size (−325 mesh powder) and one with <70 μm particle size (−200 mesh powder). These will be referred to as the −325 mesh and −200 mesh materials in the remainder of this paper. These powders were loaded into 76.2 mm (3 in) diameter extrusion cans. These were vacuum degassed at 300 °C for approximately 8 h. The cans were then blind-die compacted at 300 °C to >99% density. Subsequent extrusion to a round bar was performed at a ratio of 25:1 at 350 °C with a maximum load of approximately 26 MN.

Microstructural characterization was performed using scanning electron microscopy (SEM) and transmission electron microscopy (TEM). For SEM, samples were mounted and polished to a 1 μm finish using a diamond suspension. TEM sample preparation was done using standard electrolytic polishing in a dilute perchloric acid solution.

Tension experiments were performed at room temperature on flat bar samples of the −325 mesh and −200 mesh materials. Two samples of each material were tested. Sample dimensions were nominally 75 mm long, 2.2 mm thick, 12.4 mm wide on the ends, and 8.6 mm wide in the gage section. An extensometer with a gage length of 2.5 cm was employed. Yield strength of the material was identified at 0.2% plastic strain. All samples were tested to failure.

3. Results of microstructural analysis

Inspection by SEM revealed features resulting from consolidation of the starting powder. Fig. 1A and B show back-scattered electron SEM images
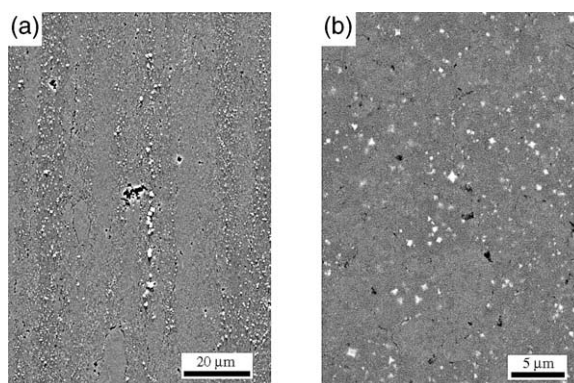

Fig. 1. SEM imaging of Al-6Mg-2Sc-1Zr alloy cross-section A) parallel to extrusion direction and B) normal to extrusion direction. Primary Al$_3$(Sc,Zr) particles, porosity, microstructural elongation and prior-particle boundaries are evident.

of cross-sections of the −325 mesh material parallel and normal to the extrusion direction, respectively. In these images, the bright, cuboidal shapes were identified as Al$_3$(Sc,Zr) crystals using electron dispersive spectroscopy (EDS). These crystals are up to 1 μm in size. The freezing range, defined as the difference between the equilibrium liquidus and solidus temperatures at a given alloy composition, increases rapidly with increasing Sc content beyond the eutectic equilibrium value of 0.5 %. At 2% Sc, the freezing range taken from the binary Al-Sc phase diagram [9] is approximately 145 °C. The solidification rate was not sufficient to suppress the formation of these primary Al$_3$(Sc,Zr) particles while cooling through this large freezing range. Porosity is also present and appears black in the images. A very low volume fraction of particles 10–20 μm in size was observed. Based on energy dispersive X-ray spectroscopy (EDX), these particles are likely Mg$_2$Al$_3$. Elongation of the microstructure in the extrusion direction is evident in Fig. 1A. Prior-particle boundaries may also be seen in Fig. 1. These boundaries exist around particles which have been deformed little or not at all during extrusion. All of these observations are evident for both the −325 mesh and −200 mesh materials.

Sample TEM dark field (DF) images of the grain structure of the −325 mesh material are shown in Fig. 2A and B. Fine equiaxed grains were observed in views parallel and perpendicular to the extrusion
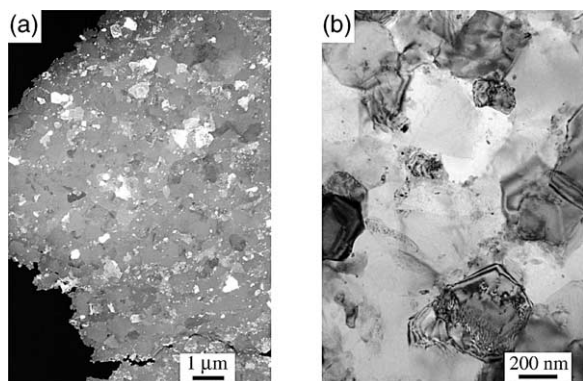
Fig. 2. TEM imaging of Al-6Mg-2Sc-1Zr alloy cross-section A) parallel to extrusion direction and B) normal to extrusion direction. Fine, equiaxed grains are observed in both views.

direction in the −325 mesh and −200 mesh materials. Average grain size for the −325 mesh and −200 mesh materials were measured as 275 and 550 nm with a standard deviation of 90 and 130 nm, respectively. These grain sizes are an average of at least 50 individually measured grain diameters on several TEM DF images. The boundaries between grains were found to be largely high-angle in selected area diffraction (SAD) observations.

The presence of fine, secondary $Al_3(Sc,Zr)$ precipitates, i.e., non-primary particles precipitated from a supersaturated solid solution, was also confirmed. The secondary $Al_3(Sc,Zr)$ particles are shown in Fig. 3. This image was formed using a
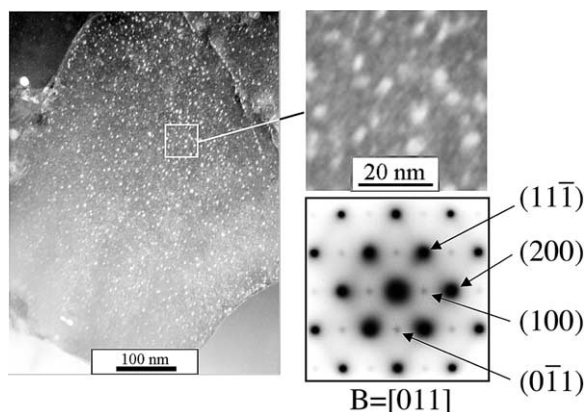

Fig. 3. TEM imaging of fine $Al_3(Sc,Zr)$ precipitates and SAD showing supperlattice reflections due to the $Al_3(Sc,Zr)$ in the Al-6Mg-2Sc-1Zr alloy.

non-standard, TEM imaging technique to excite preferentially the $(\bar{1}\bar{1}1)$ diffraction vector for the precipitates. A representative SAD pattern showing characteristic superlattice spots due to the presence of the ordered $Al_3(Sc,Zr)$ precipitates is given in Fig. 3. It is clearly shown in this figure that the secondary $Al_3(Sc,Zr)$ precipitates have a cube-on-cube orientation relationship with the Al matrix, so that these particles can be assumed to be coherent if the size of the particles and lattice constant mismatch with the matrix are not too great. The size and spacing of the fine $Al_3(Sc,Zr)$ precipitates were found to be on the nanometer scale. The average size of the $Al_3(Sc,Zr)$ precipitates was estimated from direct measurements on TEM negatives, and was determined to be about 7.5 nm.

4. Predictions of Strengthening Contributions

4.1. Solid solution strengthening

The yield strength is related to the solid solution effect by:

$$\sigma_y = \frac{3.1\varepsilon G c^{1/2}}{700} \tag{1}$$

where ε is an experimental constant, G is the shear modulus of the matrix, and c is the concentration of the solute in atomic % [11]. The shear modulus of aluminum is approximately 26 GPa [11]. To isolate the effect of the solute, yield strength may be plotted against the square root of the solute concentration. A linear fit on such a plot provides a measure of εG. Yield strengths were given by Toropova [7] for Al-Mg alloy rods extruded and annealed at 325 °C. These rods had yield strengths of 80, 115, and 130 MPa for Mg contents of 2, 5, and 6.5%, respectively. Analysis of this data provided an ε value of 3.8×10^{-7} for Mg for σ_y in MPa. A plot of the estimated strengthening of Al with Mg solute content is shown in Fig. 4. For the alloys examined in this work, the Mg was completely soluble at the extrusion temperature, although the room temperature equilibrium value in the present alloy is estimated to be below 2% [12]. Since some Mg_2Al_3 particles were observed
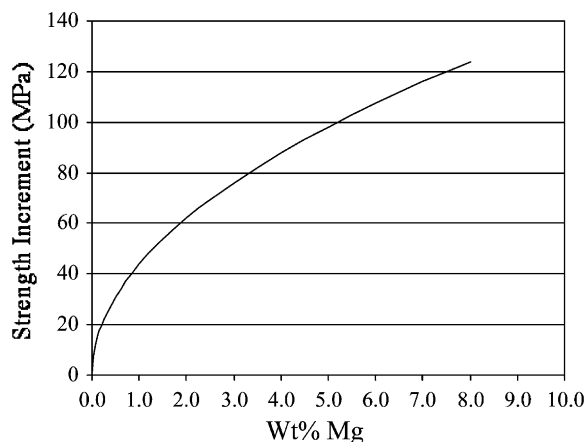
Fig. 4. Predicted strengthening increment as a function of magnesium solute content. Experimental data from Toropova [7] fall above prediction for Mg solid solution strengthening by an amount equal to the expected alloy strength without Mg.

in the consolidated material, it is clear that not all of the Mg remained in solution. Due to the infrequency of observation of these particles, it is believed that the Mg content in solution is not the equilibrium value. The Mg solute content is estimated to be in the range of 3–5 %. This concentration range corresponds to an estimated strengthening increment of 75 to 100 MPa.

The solid solubility of Sc and Zr in Al have been reported at 500 °C as 0.07 [13] and 0.05 [7] %, respectively. The equilibrium concentration is expected to decrease from these values with decreasing temperature. Due to thermal processing at and below 350 °C, the amounts of Sc and Zr in solid solution in Al-Mg-Sc-Zr materials are expected to be very low and assumed to have a negligible contribution to alloy strength due to the solid solution strengthening mechanism.

4.2. Grain boundary strengthening (Hall–Petch)

The standard Hall–Petch equation, Eq. (2), was employed to relate the yield strength of the material (σ) to the average grain size (d).

$$\sigma = \sigma_0 + kd^{-1/2} \qquad (2)$$

In this equation, σ_o is the intrinsic resistance of the lattice to dislocation motion and k is a parameter that describes the relative strengthening contri-

bution of grain boundaries. A k value of 0.17 MN/m$^{3/2}$ was used to estimate the strengthening due to grain boundaries. This value was experimentally determined for an Al-2Mg-2Li alloy [14], which is analogous to the alloys in this work due to the presence of Mg in solid solution and Li as Al$_3$Li fine precipitates. Eq. (2) was plotted with $\sigma_o = 0$ in order to isolate the grain size dependence [see Fig. 5]. Based on grain size measurement from TEM studies, the −325 mesh and −200 mesh materials are expected to have strengthening increments ranging from 280 to 395 MPa and 205 to 260 MPa, respectively.

4.3. Particle strengthening (APB/Orowan)

Strengthening of the alloy due to the fine Al$_3$(Sc,Zr) particles was analyzed using both anti-phase boundary (APB) and Orowan particle strengthening models. These models address the resistance to dislocation motion within a material due to the presence of particles. The APB model is relevant in materials with particles having an ordered structure like Al$_3$(Sc,Zr) and predicts the resistance to dislocation motion by the formation of an APB, which results from the cutting of these particles. The equation used to predict strengthening due to the APB mechanism is given in Eq. (3) [15]. Here, γ is the energy required to form the
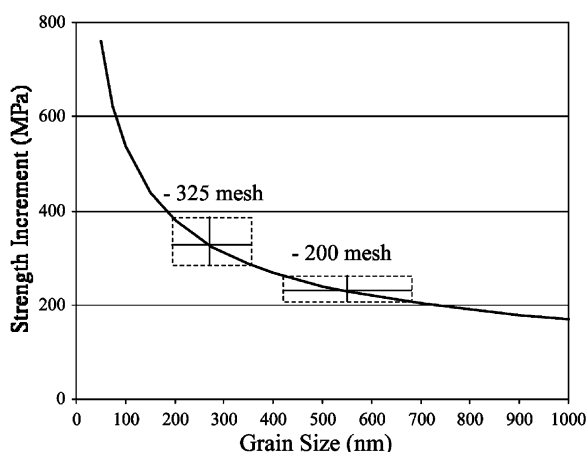

Fig. 5. Predicted strengthening due to grain size of alloy. Average measured grain size ±1 standard deviation are plotted for the −325 mesh and −200 mesh materials.

APB, b is the Burgers vector for the moving dislocations, r is the radius of the particles being cut, f is the volume fraction of particles and G is the shear modulus of the matrix. The Orowan model is also applicable to such a material and predicts dislocation motion by bowing of the dislocations around the particles. Strengthening due to the Orowan mechanism may be predicted using Eq. (4) [16]. In this equation, λ is the inter-particle spacing. At the smallest particle sizes, cutting of particles by dislocations is energetically more favorable than bowing around the particles. With increasing particle size, cutting becomes more difficult, which results in increased strengthening due to the particles. At some critical particle size, it becomes easier for dislocations to bow around the particles than to cut them. For a given volume fraction of particles, bowing around the particles becomes easier with increases in particle size, resulting in decreased strengthening. Therefore, the particle size for optimum strengthening of the material is found at the transition from the cutting mechanism to the bowing mechanism.

$$\sigma_{APB} = (3.1)\frac{\gamma^{3/2}}{b^2}\left(\frac{rf}{G}\right)^{1/2} \quad (3)$$

$$\sigma_{Orowan} = (3.1)(0.84)\frac{Gb}{\lambda} \quad (4)$$

The APB and Orowan model strengthening predictions for a range of Al$_3$(Sc,Zr) particle sizes are shown in Fig. 6. Curves are shown for three constant volume fractions of Al$_3$(Sc,Zr) particles over a range of sizes. For clarity, APB and Orowan models are only plotted to just past the intersection of the curves. The value for APB energy of Al$_3$Sc for the (111) plane has been reported as 100 to 185 mJ/m^2 from calculations based on the critical temperature for ordering and 670 mJ/m^2 using the full-potential linearized augmented plane-wave (FLAPW) method [17]. The disagreement between the reported values is not uncommon for APB energies of intermetallic compounds [17] and highlights the fundamental difficulty in accurate determination of APB energies. An APB energy of 185 mJ/m^2 was selected as a reasonable value for use in the current analyses. The particle sizes for optimum strengthening for the 1.5, 2.5, and 3.5 vol%
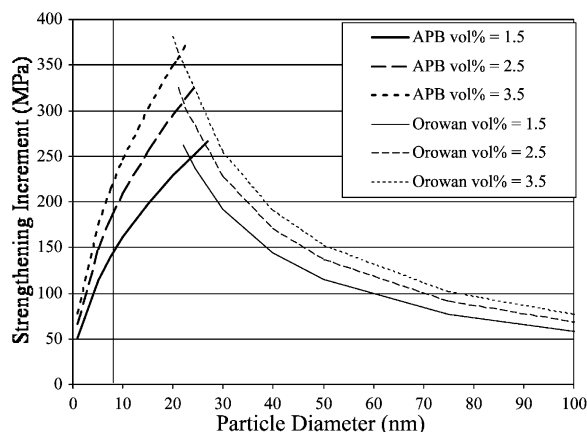

Fig. 6. Plot of APB and Orowan models for strengthening due to resistance to dislocation movement by three different volume fractions of fine particles.

materials fall between 20 and 25 nm. Measurement of the fine Al$_3$(Sc,Zr) particles in the −325 mesh and −200 mesh materials suggest an average size of approximately 7.5 nm. In this size range of particles, the particle cutting mechanism for dislocation motion is expected to be active (Fig. 6).

The volume fraction of fine, secondary Al$_3$(Sc,Zr) particles was estimated from measurements of the area fraction of primary Al$_3$(Sc,Zr) particles. Images were captured using SEM backscattered electron imaging of polished cross-sections of the as-extruded material. Gray scale images were converted to binary images by manually setting the threshold of each image, i.e., selecting the image gray level that separates the black and white pixel regimes. The large, primary Al$_3$(Sc,Zr) particles appeared white, and the remainder of the material black. The resolution of these images was approximately 200 nm, which is much larger than the observed secondary Al$_3$(Sc,Zr) particles. For this reason, all of the white pixels were assumed to be due to the primary Al$_3$(Sc,Zr) particles, and the volume fraction of these was estimated as the ratio of white to black pixels for each image. The measured volume fractions for the −325 mesh and −200 mesh materials were 0.035 and 0.045, respectively, with an error of about ±0.005. The total volume fraction of the Al$_3$(Sc,Zr) phase was calculated by adding the atomic contents of Sc and Zr, 1.5 at%, and utilizing

the published Al-Sc binary phase diagram. This yields a volume fraction of the $Al_3(Sc,Zr)$ phase of 0.06. From the measured volume fraction of the primary $Al_3(Sc,Zr)$, the volume fraction of secondary $Al_3(Sc,Zr)$ particles was estimated to be 0.025±0.005 and 0.015±0.005 for the −325 mesh and −200 mesh materials. Based on the average $Al_3(Sc,Zr)$ secondary particle size of 7.5 nm and the estimated volume fractions of those particles, the models presented in Fig. 6 show predicted strengthening of 180±20 and 140±20 MPa for the −325 mesh and −200 mesh materials, respectively.

5. Results of tensile experiments

The −325 mesh material had an average 0.2 % yield strength ($\sigma_{0.2}$) of 640 MPa with an average of 2.2% plastic ductility (ε_p), and the −200 mesh material had an average $\sigma_{0.2}$ of 540 MPa with an average ε_p of 4.1%. A plot of the stress-strain response of the 4 samples is given in Fig. 7. The duplicate tests of each material have very similar results, although the ε_p values for the −200 mesh material samples differed significantly.

The −200 mesh material exhibits a load drop, followed by serrated yielding and finally extension with little work hardening, while the −325 mesh material exhibits a load drop followed by extension with little work hardening. Observations were
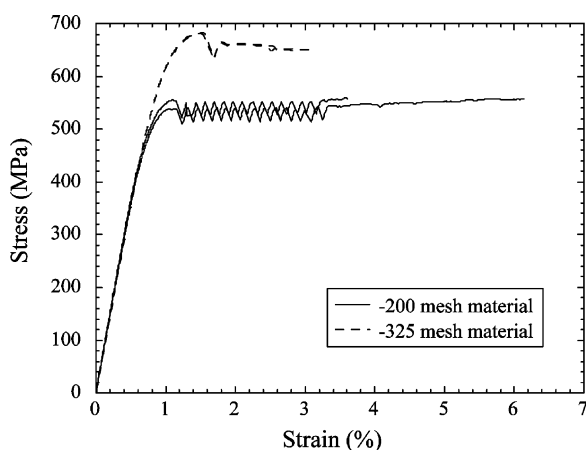
recorded of the formation and discontinuous propagation of Lüders bands along the sample during tensile testing. The load drop was found to correspond to the initial formation of a Lüders band. The serrated yielding is consistent with observations attributed to dynamic strain aging (DSA). According to the DSA theory, dislocations are temporarily immobilized by interaction with solute atoms [18]. Observation of serrated yielding attributed to DSA have been reported in a number of alloy systems, including Al-Mg alloys. Similar behavior to that observed here has been reported for an Al-5Mg alloy [18].

Post-test examination of the fracture surfaces was performed. Fracture surfaces of both materials exhibited fine dimples indicating ductile rupture (Fig. 8). Each of the samples tested exhibited one of two types of fracture initiation sites. Fig. 9 shows lower and higher magnification SEM images of a failure initiated at an undeformed prior-particle. Rivermarks point very clearly to the prior powder particle near the surface of the tensile bar. This approximately 30 μm diameter particle is nearly spherical and therefore remained largely undeformed despite consolidation processing. Fracture initiated at the particle-matrix interface. A matching hemispherical hole was observed in the opposing fracture surface. EDX of the particle did not reveal any significant compositional difference from the matrix. Fig. 10 also has clear rivermarks pointing to the initiation site. In this case, fracture was initiated at a brittle particle roughly 30 μm in

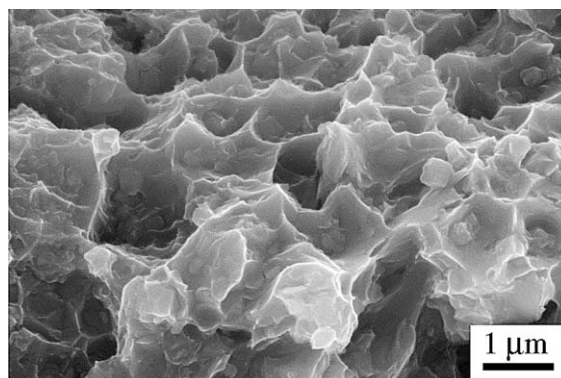Fig. 7. Stress-strain response of tested tensile samples.

Fig. 8. Secondary electron SEM image of dimples on tensile fracture surface.
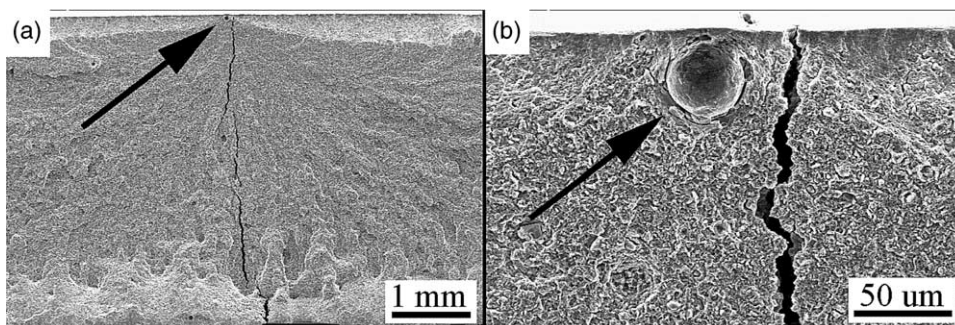
Fig. 9. Secondary electron SEM images illustrating fracture initiation at a prior-particle boundary. A) rivermarks may be traced back to fracture origin B) undeformed powder particle.
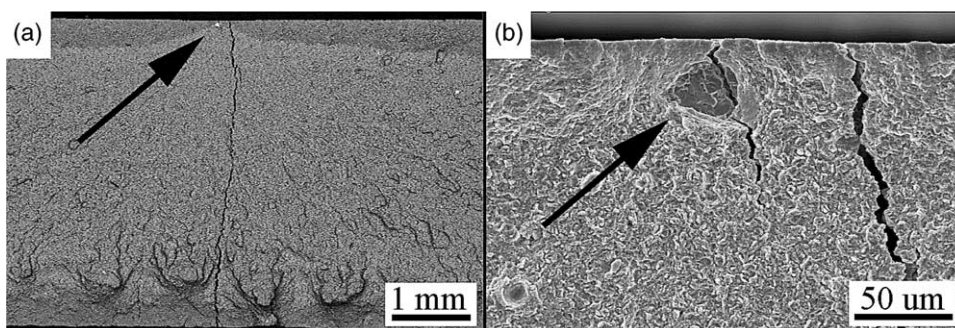

Fig. 10. SEM images of fracture initiation at an Fe-rich particle. A) backscattered electron imaging shows Fe-rich particle as bright spot B) secondary electron image of fractured, Fe-rich particle.

size. EDX identified this particle as an Fe-rich impurity.

6. Comparison of results from models and experiments

The predictions of strengthening contributions are compared to experimental results in Table. 1. The yield strength of 99.99% pure Al is 10 MPa [21], which is only a very small contribution to the alloy strength. Model predictions suggest that strengthening due to grain boundaries is the most significant contributor to the strength of both the −325 mesh and -200 mesh materials, followed in decreasing order of significance by strengthening due to secondary $Al_3(Sc,Zr)$ particles and solid solution strengthening by Mg.

A linear summation of the strengthening mechanisms was found to give very good agreement

Table. 1
Predicted strengthening compared to experimental results.

Strengthening Contribution	−325 mesh material (MPa)	−200 mesh material (MPa)
Pure Al strength	10	10
Solid solution strengthening	75–100	75–100
Grain boundary strengthening	280–395	205–260
Secondary particle strengthening	160–200	120–160
Total predicted strength	**525–705**	**410–530**
Experimental yield strength	**640**	**540**

between the predicted and experimentally measured strengths for both the −325 and −200 mesh materials. This suggests that there is no interaction between strengthening mechanisms in this alloy. Eq. (5) has been used to describe the summation of strengthening contributions by different mechanisms [19], where τ is the critical resolved shear stress and τ_i represents the individual contribution to τ by each mechanism. A linear summation corresponds to a k of 1. This equation has been used to describe the superposition of strengthening mechanisms for a Ni-based superalloy with solid solution and coherent precipitate strengthening using a k of approximately 1.1 [19] and for Ni-rich Ni-Al alloys with a bimodal size distribution of Ni_3Al precipitates using a k of approximately 1.6 [20], in good agreement with results in this work.

$$\tau^k = \sum \tau_i^k \qquad (5)$$

7. Discussion

The agreement between the predictions for strengthening and experimental results is good. For the −325 mesh material, the experimental result falls well within the estimated strengthening range, and for the −200 mesh material, the experimental result exceeds the predicted range by only 10 MPa. Other potential sources of strengthening include work hardening, oxide particles from prior-particle surfaces, Mg_2Al_3 particles due to limited solubility of Mg, Fe-rich impurities, primary $Al_3(Sc,Zr)$ particles, dissolved hydrogen due to incomplete degassing, and solid solution strengthening by Sc and Zr. Work hardening is not expected to be significant based on the scarcity of dislocations observed during TEM examinations of these materials. The Mg_2Al_3 particles, Fe-rich inclusions and primary $Al_3(Sc,Zr)$ particles were all observed to exist as relatively large particles. Because the volume fractions of these large particles is likely much less than 5% in each case, strengthening by these particles is expected to be small. Hydrogen is known to reduce the fracture properties of Al alloys due to a higher solubility in the liquid at the melting point than in the solid at the same temperature [22]. The potential contribution to strength by

dissolved hydrogen is difficult to predict. Solid solution strengthening by Sc and Zr is expected to be very small due to the extremely low equilibrium solubility of these at and below the temperatures used for degassing, compaction, and consolidation. The good agreement between the predictions and the experimental results also suggests that any strengthening by other sources is a relatively small contribution to the strength of the alloy.

The −325 mesh starting powder resulted in a consolidated material with a finer grain size and larger volume fraction of secondary $Al_3(Sc,Zr)$. Smaller powder particle sizes experience higher cooling rates during the atomization process, and the as-solidified structure becomes finer due to the decreasing time allowed for diffusional processes. The metastable solubility of Sc and Zr is also expected to increase with increasing cooling rate. Examination of polished cross-sections of the Al-6Mg-2Sc-1Zr starting powder particles revealed that the volume fraction of primary $Al_3(Sc,Zr)$ particles decreased with particle size and was nearly zero below a particle size of approximately 20 μm [23]. The additional Sc and Zr solutes are expected to precipitate $Al_3(Sc,Zr)$ particles in subsequent thermal-mechanical processing. In order to achieve higher strength in these alloys, it is advantageous to use the highest possible cooling rates in order to increase the supersaturation of Sc and Zr, and hence to increase the volume of fine $Al_3(Sc,Zr)$ particles. This can effectively be achieved by using the smallest possible powder size fractions.

The analysis of secondary particle strengthening using APB and Orowan models reveals strategies for increasing the strength of this alloy. From the calculations plotted in Fig. 6, the particle size for optimum strengthening ranges from 20 to 25 nm for secondary $Al_3(Sc,Zr)$ volume fractions of 0.015–0.035. To achieve the optimum particle size, the current materials would require significant growth of the $Al_3(Sc,Zr)$ particles. It may be possible to achieve the desired coarsening without introducing unwanted effects, such as grain growth, through an appropriate heat treatment of the alloy. By increasing the fine $Al_3(Sc,Zr)$ particle size from the current value of 7.5 nm to the optimum value, a total contribution of 315 MPa to the strength of the material due to particle strengthen-

ing is predicted for a 0.025 volume fraction of secondary $Al_3(Sc,Zr)$ particles, which is an increase of approximately 135 MPa over the -325 mesh material.

The advantage of increasing the volume fraction of fine $Al_3(Sc,Zr)$ is also illustrated by this analysis. By increasing the secondary $Al_3(Sc,Zr)$ volume fraction from 0.015 to 0.035 at the optimum particle size, an additional strength increase of 100 MPa is predicted. Adding Sc beyond the current value of 2% would likely not increase the volume fraction of fine $Al_3(Sc,Zr)$, since this would significantly increase the freezing range of the material [9]. Given the rapid growth rate of primary particles in a highly undercooled melt, it is likely that the volume fraction of secondary $Al_3(Sc,Zr)$ would decrease due to the increased freezing range in alloys with higher Sc content. By instead decreasing the Sc content from 2% to 1%, the freezing range would decrease from approximately 145 ° to 90 °C. If this decrease in freezing range allows the suppression of the nucleation of primary $Al_3(Sc,Zr)$, a volume fraction of fine $Al_3(Sc,Zr)$ particles of 0.035 will be produced, which is 40% higher than the volume fraction of 0.025 obtained in the current 2% Sc, -325 mesh powder. This analysis predicts that an Al-6Mg-Sc-Zr alloy with a 0.035 volume fraction of fine $Al_3(Sc,Zr)$ particles with the optimum size will have a tensile yield strength of up to 865 MPa (125 ksi).

There is potential for increasing tensile ductility of the Al-Mg-Sc-Zr alloy. It was identified that the Fe-rich particles, which in some cases acted as fracture initiation sites, resulted from impurities introduced during melting of the alloy prior to atomization. This should be eliminated by controlled production practices. Chemical analysis of the -325 mesh and -200 mesh materials revealed an average of 170 and 50 ppm of hydrogen, respectively. Hydrogen is known to be detrimental to ductility of aluminum alloys due to dissolution of hydrogen gas upon solidification [22], and observed porosity may accentuate this. The increased hydrogen content did correlate with decreased ductility. EDX of the undeformed powder particles did not reveal any significant compositional difference from the matrix. The oxide layer

at the surface of the particle may have increased the stress required to deform the particle a sufficient amount to prevent deformation of the particle during extrusion. Optimized degassing of the starting powder will assist in breaking up the surface oxide layer prior to compaction and extrusion, which will help achieve uniform deformation of the powder particles. This, coupled with optimization of extrusion temperature and reduction ratio to produce sufficient shearing of the material, will ensure that prior-particle boundaries are minimized.

8. Conclusions

- Tensile yield strengths of Al-6Mg-2Sc-1Zr (wt%) (Al-6.7Mg-1.2Sc-0.3Zr (at%)) alloys at room temperature ranged from 540 to 640 MPa. Calculations suggest that grain boundary strengthening is the largest contributor to the strength, while APB strengthening and solid solution strengthening also contribute significantly.
- There is good agreement between model predictions of alloy strengths and experimentally measured values, and calculations suggest that there is no interaction between strengthening mechanisms.
- Smaller starting powder size results in a significantly smaller grain size and larger volume fraction of fine $Al_3(Sc,Zr)$ particles with a corresponding increase in alloy strength. The larger volume fraction of fine $Al_3(Sc,Zr)$ is likely a result of the higher relative cooling rate experienced by the smaller powders.
- The strengthening models show that the strength of these alloys could be significantly enhanced by increasing the $Al_3(Sc,Zr)$ particle size from the currently observed values of ~7.5 nm to the optimum size range, 20–25 nm. For a material with a volume fraction of 0.025 of secondary $Al_3(Sc,Zr)$ particles, an increase in strength of 135 MPa is predicted by effecting this change. This may be achievable by heat treatment.
- The strengthening models show that the strength of these alloys could be significantly increased by increasing the volume fraction of fine $Al_3(Sc,Zr)$ particles to 0.035. By increasing the

secondary Al$_3$(Sc,Zr) volume fraction from 0.015 to 0.035 at the optimum particle size, an additional strength increase of 100 MPa is predicted.

- It may be possible to increase the secondary Al$_3$(Sc,Zr) volume fraction by decreasing the Sc content of the alloy from 2 wt% to 1 wt%, thus decreasing the solidification freezing range.
- Tensile plastic ductility at room temperature averaged from 2 to 4%. Prior-particle boundaries and Fe-rich particles act as tensile fracture initiation sites and interstitial hydrogen and porosity likely limit ductility. Minimization of these extrinsic defects by optimization of degassing of the starting powder and of deformation parameters should provide an increase in ductility of the alloy.

Acknowledgements

References

[1] Kim Y-W. In: Kim Y-W, Griffith WM, editors. Dispersion Strengthened Aluminum Alloys. TMS Publishing; 1988. p. 15-7.

[2] Skinner DJ. In: Kim Y-W, Griffith WM, editors. Dispersion Strengthened Aluminum Alloys. TMS Publishing; 1988. p. 18-1.

[3] Leng Y, Porr WC, Gangloff RP. Scripta Metal & Mat 1990;24:2163.

[4] Sawtell RR, Morris JW. In: Kim Y-W, Griffith WM, editors. Dispersion Strengthened Aluminum Alloys. TMS Publishing; 1988. p. 40-9.

[5] Angers LM, Konitzer DG, Murray JL, Truckner WG. In: Kim Y-W, Griffith WM, editors. Dispersion Strengthened Aluminum Alloys. TMS Publishing; 1988. p. 35-5.

[6] Gschneidner KA, Calderwood FW. In: Okamoto H, Subramanian PR, Kacprzak L, editors. Binary Alloy Phase Diagrams. ASM Publishing; 1990. p. 20-8.

[7] Toropova LS, Eskin DG, Kharakterova ML, Dobatkina TV. Advanced Aluminum Alloys Containing Scandium. Publishing: Gordon and Breach, 1998.

[8] Yin Z, Pan Q, Zhang Y, Jiang F. Mat Sci Engr A 2000;280:151.

[9] Sawtell RR, Jensen CL. Met Trans A 1990;21A:421.

[10] Ünal R, Kainer KU. Powder Metal 1998;41:119.

[11] Hertzberg RW. Deformation and Fracture Mechanics of Engineering Materials 3rd ed. Wiley Publishing, 1989.

[12] Murray JL. In: Okamoto H, Subramanian PR, Kacprzak L, editors. Binary Alloy Phase Diagrams. ASM Publishing; 1990. p. 16-9.

[13] Fujikawa SJ, Sugaya M, Takei H, Hirano KI. J Less-Common Met 1979;63:87.

[14] Dinsdale K, Harris SJ, Noble B. Aluminum Lithium Alloys. In: Sanders TH, Starke EA, editors. TMS proceedings. 1981. p. 10-1.

[15] Ham RK. 3rd Bolton Landing Conference, Kear BH., Sims CT., Stoloff NS., Westbrook JH., editors, 1969; p365.

[16] Hull D, Bacon DJ. Introduction to Dislocations, 3rd ed. Pergamon Press, 1984.

[17] Westbrook JH, Fleischer RL, editors. Intermetallic Compounds: Principles and Practice, vol. 1. Wiley publishing; 1995. p. 50-5.

[18] Robinson JM, Shaw MP. Intl Mat Rev 1994;39:113.

[19] Schänzer S, Nembach E. Acta Metall Mater 1992;40:803.

[20] Chellman DJ, Luévano AJ, Ardell AJ. In: Brandon DG, Chaim R, Rosen A, editors. Proc. 9th Int. Conf On the Strength of Metals and Alloys. 1991. p. 53-7.

[21] Smith WF. Structure and Properties of Engineering Alloys. McGraw-Hill Publishing, 1981.

[22] Hatch JE, editor. Aluminum: Properties and Physical Properties. ASM publishing; 1984. p. 22-9.

[23] Pandey AB., Kendig KL., Miracle DB. Affordable MMC's for High Performance Applications. In: Pandey AB, Kendig KL, Watson TA, editors. TMS proceedings, Nov. 2001 (submitted).